Simulation of Vickers indentation of silica glass

Mohamed Jebahi, Damien André, Frédéric Dau, Jean-Luc Charles, Ivan Iordanoff

Simulation of Vickers indentation of silica glass.

Mohamed JEBAHI[a,*], Damien ANDRÉ[b], Frédéric DAU[b], Jean-luc CHARLES[b], Ivan IORDANOFF[b]

[a]Univ. Bordeaux, I2M, UMR 5295, F-33400 Talence, France
[b]Arts et Metiers ParisTech, I2M, UMR 5295 CNRS F-33400, Talence, France

Abstract

The indentation response of glasses can be classified under three headings: normal, anomalous and intermediate, depending on the deformation mechanism and the cracking response. Silica glass, as a typical anomalous glass, deforms primarily by densification and has a strong tendency to form cone cracks that can accompany median, radial and lateral cracks when indented with a Vickers tip. This is due to its propensity to deform elastically by resisting plastic flow. Several investigations of this anomalous behavior can be found in the literature. The present paper serves to corroborate these results numerically using the discrete element method. A new pressure-densification model is developed in this work that allows for a quantitative estimate of the densification under very high pressure. This model is applied to simulate the Vickers indentation response of silica glass under various indentation forces using the discrete element method first, and then a discrete-continuum coupling method with large simulation domains to suppress the side effects and reduce the computational time. This coupling involves the discrete element method (DEM) and the constrained natural element method (CNEM). The numerical results obtained in this work compare favorably with past experimental results.

Keywords: Brittle, Amorphous, Glassy silica, Densification, Fracture, Indentation, Discrete elements, discrete-continuum coupling

1. Introduction

Because of their excellent physical (i.e. mechanical, thermal and optical) properties in addition to excellent chemical resistance, several types of glasses have become the main focus of several researchers. According to the dependence of various properties such as density, hardness, refractive index, Young's and shear moduli with the pressure and fictive temperature (defined in a simple manner as the temperature at which the glass would be in thermal equilibrium), glasses can be classified under three headings: normal, intermediate and anomalous. Normal glasses, such as soda-lime silicate glass, exhibit properties decreasing with increasing fictive temperature and pressure. Anomalous glasses, such as germania, exhibit the opposite trend in these properties. Intermediate between normal and anomalous glasses are expected to have some properties that are independent of these parameters (i.e. pressure and fictive temperature). Of particular interest is silica glass which is known to exhibit anomalous behavior in its thermal and mechanical properties [1, 2]. Furthermore, certain properties of this type of glass such as the Young's and shear moduli and the density show an anomalous dependence on the fictive temperature. When indented with a Vickers tip, silica glass exhibits a cracking pattern that is more complex than in a typical normal glass, such as soda-lime silicate [3, 4]. Specifically, silica glass has a strong tendency to form ring cracks at the periphery of the indenter impression, but other crack systems typical of normal glasses, i.e. median, radial and lateral cracks, can be introduced [5, 6]. The anomalous cracking response in silica glass is due to its propensity to deform elastically by resisting inelastic flow. In the region of ordinary hydrostatic pressures (up to approximately 8 GPa), silica glass behaves in a perfectly elastic manner. However, and contrary to crystalline solids, when the hydrostatic pressure is in the 8 GPa range or beyond, silica glass begins to exhibit signs of permanent deformation. The permanent

---

*Corresponding author
Email address:* `mohamed.jebahi@u-bordeaux1.fr` (Mohamed JEBAHI)

deformation of silica glass, which is an amorphous solid, is very different from the plastic flow found in crystalline solids. Indeed, the plastic flow in crystalline solids is volume-conservative and initiates under shear stress only. The spherical part of the stress tensor has no influence on the plastic flow. However, the permanent deformation of silica glass is always accompanied by a volume change. In addition, as found in several previous works [7, 8, 9, 10], it can initiate under hydrostatic pressure. There are several works on this subject in the literature, some of which are controversial. It began with the works of Bridgman and Šimon [7]. They demonstrated that amorphous silica exhibits permanent densification which translates to a permanent volume decrease of approximately 7.5 % at approximately $20\,GPa$. They also demonstrated that this propensity decreases when other substances are added, such as sodium oxide, Na_2O. However, at that time, technical difficulties prevented the generation of strictly hydrostatic conditions at pressures above $5\,GPa$ [7]. Uniaxial pressures were applied on thin disks to study the densification of glasses. Unfortunately, these tests induced additional shear stresses, which explain the systematic fracturing of the samples.

Cohen and Roy [11] studied the densification of silica powder under uniaxial pressures. They found that the densification begins at approximately $2\,GPa$ ($10\,GPa$ in Bridgman and Šimon's work [7]) and the volume reduction can far exceed 7.5 %. According to Reference [12], the difference between the previous results is due to the shearing effects, which are most important in the case of silica powder and allows a greater densification level to be reached. This explanation was belied later by Cohen and Roy [13], who excluded the shearing effects on the densification level. For more details, the reader can refer to [14]. Several other works treating the shearing effects can be found in the literature [15, 16, 17]. At present, this subject has not been resolved, and the role of the shearing stresses in densification remains ambiguous.

In the present work, the densification of silica glass is studied numerically using a discrete element method developed by André *et al.* [18, 19] for brittle continuous media. A new densification model based on the compressive stress in the cohesive bonds between the neighboring discrete elements is proposed. As will be shown later, this model provides a relatively good quantitative estimate of silica glass densification under high hydrostatic pressure (in comparison to previous numerical studies [8]). Subsequently, the influence of the densification on the cracking response of silica glass indented with a Vickers tip is investigated using a new fracture model recently developed by André *et al.* [20]. This model, based on the notion of virial stress [21, 22], accurately simulates the cracking mechanisms at both the macroscopic and microscopic scales.

This paper is organized as follows: in Section 2, the elastic model of silica glass is briefly reviewed. Subsequently, the densification model developed in this work is presented. Then, the calibration procedure using hydrostatic compression on thick samples (spheres) is detailed. Section 3 reviews the fracture model used to model the cracking behavior of silica glass indented with a Vickers tip. In Section 4, the Vickers indentation process in silica glass is simulated using the discrete element method first, and then the discrete-continuum coupling method, between the discrete element method (DEM) and the constrained natural element method (CNEM) [23], is introduced to reduce the side effects and the computational time. Low indentation forces are applied, initially, to study the densification behavior in the absence of fracturing. Next, high indentation forces are applied to study the influence of densification on the cracking behavior. Section 5 presents the conclusions.

2. Silica behavior modeling

2.1. Elasticity

The variation of the discrete element method (DEM) used here is that developed by André *et al.* [18] and implemented in the GranOO workbench (software)[1]. The elastic behavior of silica glass is modeled using cylindrical elastic "cohesive beams" having geometric (length l_μ and dimensionless radius $\tilde{r}_\mu$, defined as the ratio of the beam radius to the mean particle radius) and mechanical properties (Young's modulus E_μ and Poisson's ratio ν_μ) between the adjacent discrete elements (**Fig. 1**).

The Euler-Bernoulli analytical model of a beam [24] is used to compute the beam forces and torques on the discrete elements connected to this beam ((1), (2), (3) and (4)). Hereafter, the subscript "μ" denotes microscopic quantities.
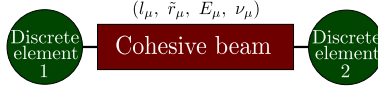
---

[1]http://www.granoo.org

Figure 1: Elastic beam model between two adjacent discrete elements

Table 1: The microscopic elastic parameters of silica glass (obtained by calibration)

Young's Modulus	Poisson's ratio	Dimensionless radius
$E_\mu = 414\,GPa$	$\nu_\mu = 0.3$	$\tilde{r}_\mu = 0.57$

$$\boldsymbol{F}_\mu^{DE1} = +E_\mu S_\mu \frac{\Delta l_\mu}{l_\mu}\boldsymbol{x} + \frac{6E_\mu I_\mu}{l_\mu^2}(-(\theta_{2z} + \theta_{1z})\boldsymbol{y} + (\theta_{2y} + \theta_{1y})\boldsymbol{z}) \tag{1}$$

$$\boldsymbol{F}_\mu^{DE2} = -E_\mu S_\mu \frac{\Delta l_\mu}{l_\mu}\boldsymbol{x} - \frac{6E_\mu I_\mu}{l_\mu^2}(-(\theta_{2z} + \theta_{1z})\boldsymbol{y} + (\theta_{2y} + \theta_{1y})\boldsymbol{z}) \tag{2}$$

$$\boldsymbol{T}_\mu^{DE1} = +\frac{G_\mu Io_\mu}{l_\mu}(\theta_{2x} + \theta_{1x})\boldsymbol{x} - \frac{2E_\mu I_\mu}{l_\mu}((\theta_{2y} + 2\theta_{1y})\boldsymbol{y} + (\theta_{2z} + 2\theta_{1z})\boldsymbol{z}) \tag{3}$$

$$\boldsymbol{T}_\mu^{DE2} = -\frac{G_\mu Io_\mu}{l_\mu}(\theta_{2x} + \theta_{1x})\boldsymbol{x} - \frac{2E_\mu I_\mu}{l_\mu}((2\theta_{2y} + \theta_{1y})\boldsymbol{y} + (2\theta_{2z} + \theta_{1z})\boldsymbol{z}) \tag{4}$$

Where:

- $R(\boldsymbol{x}, \boldsymbol{y}, \boldsymbol{z})$ is the beam local frame where $\boldsymbol{x}$ is the beam axis.

- $\boldsymbol{F}_\mu^{DE1}$ and $\boldsymbol{F}_\mu^{DE2}$ are the beam force reactions acting on discrete elements 1 and 2 (connected to this beam bond).

- $\boldsymbol{T}_\mu^{DE1}$ and $\boldsymbol{T}_\mu^{DE2}$ are the beam torque reactions acting on discrete elements 1 and 2.

- l_μ and Δl_μ are the initial beam length and the longitudinal deflection.

- $\boldsymbol{\theta}_1(\theta_{1x}, \theta_{1y}, \theta_{1z})$ and $\boldsymbol{\theta}_2(\theta_{2x}, \theta_{2y}, \theta_{2z})$ are the rotations of the beam cross sections expressed in the beam local frame.

- S_μ, Io_μ and I_μ are the beam cross-sectional area, the polar moment of inertia and the moment of inertia with respect to the $\boldsymbol{y}$ and $\boldsymbol{z}$ axes, respectively.

- E_μ and G_μ are the Young's and shear moduli, respectively.

Table 1 presents the microscopic elastic cohesive beam properties that produce the expected macroscopic elastic behavior of silica glass. These properties have been determined by calibration tests as explained in Reference [18].

2.2. Densification

2.2.1. Densification model

This subsection details how the densification behavior of silica glass is modeled. As explained in Section 1, several studies examined the densification of glasses, in particular silica glass. Nearly all previous studies agreed that this behavior takes place under high hydrostatic pressures. However, the effects of shearing on this phenomenon remain a central issue of several scientific studies on glasses.
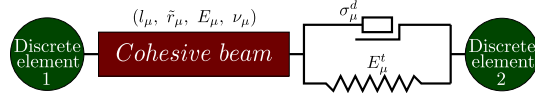
Figure 2: Densification model between two adjacent discrete elements

In this work, it is assumed that the effects of shearing on the densification are insignificant and these are dominated by the hydrostatic pressure effects. Therefore, densification of silica glass will be supposed to occur only under high hydrostatic pressures. There are many physical and mechanical reasons that support this assumption:

- According to the characteristics of materials, two main mechanisms can explain a permanent deformation due to shear stresses: (i) In the case of crystalline solids, plasticity is due to dislocation slip, defined as crystallographic defects within the crystalline structure. Silica glass which is an amorphous material lacks the long-range order characteristic of a crystal. Therefore, it is very difficult for dislocation to develop and move within its irregular structure [25]. (ii) In the case of brittle materials, such as rock and concrete, permanent deformation is caused predominantly by slip at micro-cracks. This generally weakens the material in question and degrades its mechanical properties [26]. That is not the case for silica glass. In fact, permanent deformation in silica glass enhances the mechanical properties [8, 14].

- Because silica glass is an isotropic material, permanent deformation due to shear stress is volume-conservative. Therefore, even if a shear stress can cause silica glass plasticity, this does not affect the densification level (volume change at given pressure). For an infinitesimal strain, the volume change can be expressed as:

$$\frac{dV}{V_0} = J - 1 \cong trace(\boldsymbol{\varepsilon})$$

where dV is the volume change, V_0 is the initial volume, J is the determinant of the Jacobian matrix and $\boldsymbol{\varepsilon}$ is the strain tensor. If only shear stresses are applied, $trace(\boldsymbol{\varepsilon}) = 0$, and therefore $dV = 0$.

Based on the previous assumption (the shearing effects on the densification are insignificant compared with those of hydrostatic pressure), a densification model adapted for discrete element models is developed in this work. A "spring-slider" system is connected in series with each cohesive beam linking two particles, as shown in Figure 2. When the compression stress in the associated beam σ_{beam}^c reaches the microscopic densification pressure σ_μ^d, the slider activates and the densification mechanism takes place. The densification level beyond σ_μ^d is controlled by the microscopic tangential modulus E_μ^t, which is adjustable (**Fig. 3**). Finally, to model the saturation stage, the slider stops slipping above a certain limit controlled by the maximum microscopic permanent deformation of cohesive bonds $\varepsilon_\mu^{p\,max}$.

As shown in the literature [8, 14, 27], the macroscopic mechanical properties of silica glass increase with densification. According to Ji [8], Young's modulus (E) and Poisson's ratio (v) increase by 46% and 56%, respectively, at the end of the densification process (**Fig. 4**). For the sake of simplicity, in the present work, the variations in these two parameters with hydrostatic pressure (**Fig. 4**) are approximated by linear piecewise functions. The mechanical properties remain constant until the densification pressure P_d is reached, then increase linearly between P_d and P_s (the saturation pressure) and remain constant above P_s.

To take into account the macroscopic mechanical properties dependence with pressure in the densification model, it is necessary to find the variations in the microscopic cohesive beam properties, which implies such macroscopic variations. In other words, it is necessary to find relationships between the macroscopic and microscopic (of cohesive beams) mechanical properties. Based on the work of André *et al.* [18], the following conclusions can be drawn:

- The microscopic Poisson's ratio of cohesive beams v_μ has no influence on the macroscopic elastic behavior. The latter depends only on the dimensionless cohesive beam radius $\tilde{r}_\mu$ and the microscopic Young's modulus E_μ.
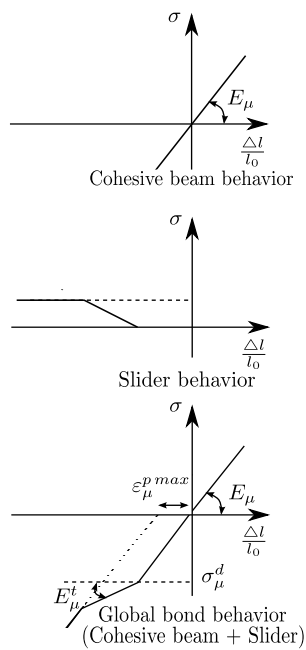
4

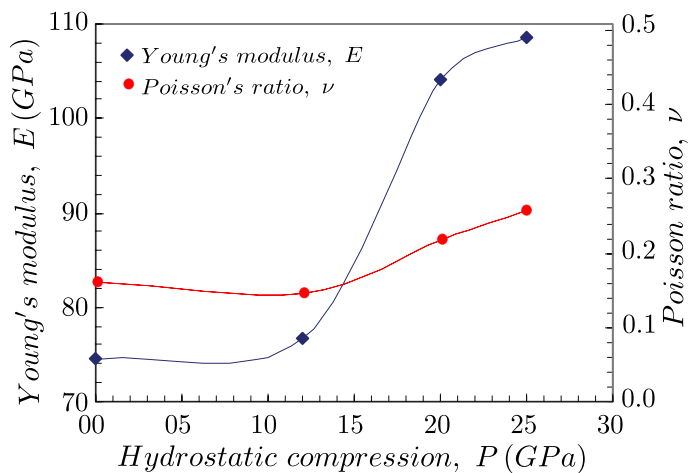Figure 3: Equivalent cohesive bond behavior

Figure 4: Variations in mechanical properties with densification (taken from the experimental works of Ji [8])
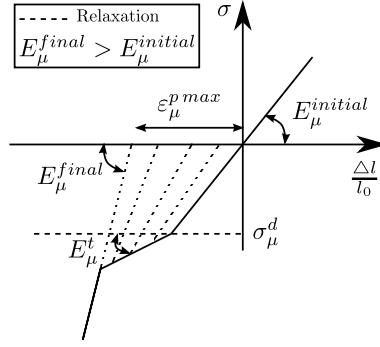
Figure 5: Behavior of equivalent cohesive bond, taking into account the variation of the mechanical properties with densification

- The macroscopic Poisson's ratio ν depends only on $\tilde{r}_\mu$. The function relating these two parameters may be approximated by a second-order polynomial.

- The macroscopic Young's modulus E is a function of both $\tilde{r}_\mu$ and E_μ. For a given value of $\tilde{r}_\mu$, E depends linearly on E_μ, whereas it is a second-order function of $\tilde{r}_\mu$ for a constant E_μ.

According to these facts, the relationships between the microscopic and macroscopic parameters can be written as in (5) and (6):

$$\tilde{r}_\mu = a_0 + a_1\nu + a_2\nu^2 \tag{5}$$

$$\begin{cases} E(E_\mu, \tilde{r}_\mu) &= b_0(\tilde{r}_\mu) + b_1(\tilde{r}_\mu)\, E_\mu \\ b_0(\tilde{r}_\mu) &= b_{00} + b_{01}\tilde{r}_\mu + b_{02}\tilde{r}_\mu^2 \\ b_1(\tilde{r}_\mu) &= b_{10} + b_{11}\tilde{r}_\mu + b_{12}\tilde{r}_\mu^2 \end{cases} \tag{6}$$

The various parameters of Equations (5) and (6) were determined by calibration tests. Knowing of these relationships ((5) and (6)), the variations of the microscopic properties of silica glass with pressure can be determined and taken into account in the densification model. Figure 5 presents the cohesive bond behavior taking into account the variation of the microscopic mechanical properties with densification. As can be shown in this Figure, the relaxation slope (current microscopic Young's modulus) increases with the densification state.

2.2.2. Calibration of the microscopic densification parameters

The densification model involves three microscopic parameters which are the microscopic densification pressure σ_μ^d, the microscopic tangential modulus E_μ^t and the maximum permanent deformation of the beam bonds $\varepsilon_\mu^{p\,max}$. The macroscopic densification parameters are the densification pressure P_d, the saturation pressure P_s and the volume change ratio $\frac{\Delta V}{V_0}$ (or density change ratio $\frac{\Delta\rho}{\rho_0}$). Several studies have measured the densification of silica glass, and different values of the macroscopic densification parameters can be found in the literature (**Table 2**). In the present work, Ji's results [8], which were obtained using thick samples, are used (**Table 2**) (because Ji conducted a complete experimental study of densification and Vickers indentation for several types of glasses).

In this section, the microscopic densification parameters will be calibrated numerically to find the desired macroscopic densification behavior. A $100\,mm$-diameter sphere model (thick model) subjected to hydrostatic compression is used for the calibration study.

One major problem of the discrete methods is the dependence of results on the discrete element number (N_p) used to discretize the numerical sample. Therefore, the influence of this parameter on the densification response is first studied. The sphere model was discretized using various numbers of discrete elements N_p (from 100 to 20 000). The microscopic densification parameters were fixed as follows: the microscopic densification pressure $\sigma_\mu^d = 5\,GPa$, the microscopic tangential modulus $E_\mu^t = 0\,GPa$ and the maximum permanent deformation of the beam bonds $\varepsilon_\mu^{p\,max} = 0.05$. Figure 6 presents the results of this study. For a small number of discrete elements (N_p), the densification response fluctuates greatly with this parameter (**Fig. 6a**). These fluctuations can be reduced

Table 2: Macroscopic densification parameters of silica glass

	Densification pressure, P_d	Saturation pressure, P_s	Volume change, $\frac{\triangle V}{V_0}$
Literature [1, 2, 14, 35, 36]	$5.9 - 10\,GPa$	$20 - 30\,GPa$	17.4 %
Ji [8]: retained parameters in this work	$8\,GPa$	$20\,GPa$	17.4 %

(a) Small number of discrete elements (N_p)
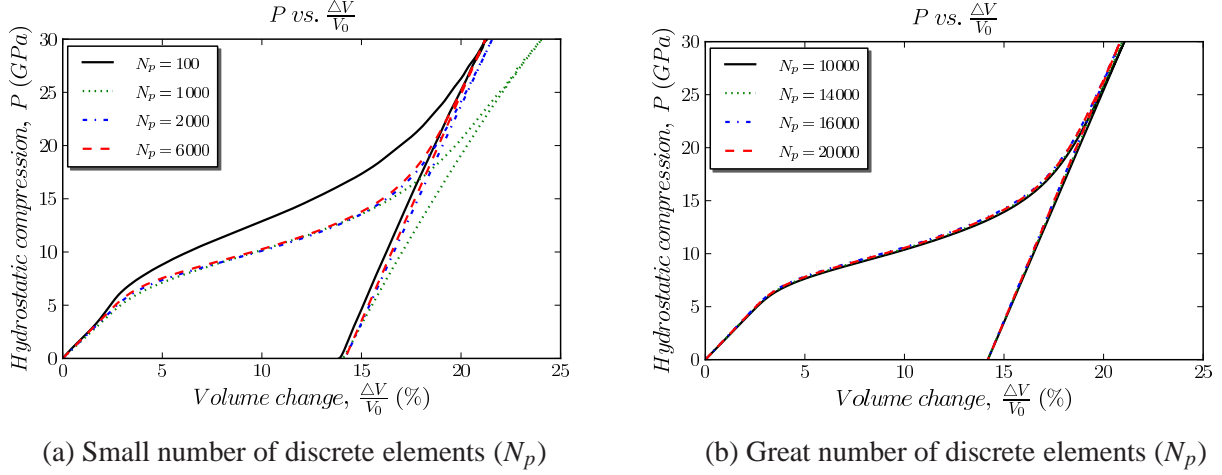
(b) Great number of discrete elements (N_p)

Figure 6: Sensitivity of the macroscopic densification behavior to the number of discrete elements (N_p)

by increasing N_p. Beyond $N_p = 10\,000$, the densification response becomes very weakly affected by the discrete element number (**Fig. 6b**).

In the remainder of this section, $N_p = 10\,000$ discrete elements will be used to discretize the numerical samples. To simplify the calibration process, the influence of the microscopic densification parameters on the macroscopic silica behavior is studied. Figure 7a shows that the macroscopic densification pressure P_d depends linearly on the microscopic one σ_μ^d. In addition, as observed in Figures 7b and 7c, this parameter is effectively independent of the other microscopic properties, i.e. E_μ^t and $\varepsilon_\mu^{p\,max}$.

Figure 8 shows the influence of the various microscopic parameters on the macroscopic saturation pressure P_s. This parameter depends linearly on the microscopic densification pressure σ_μ^d, and it depends on the microscopic tangential modulus E_μ^t (around 12% variation for E_μ^t up to $100\,GPa$). However, it is effectively independent of the maximum permanent deformation of the beam bonds $\varepsilon_\mu^{p\,max}$ (**Fig. 8c**), only 5% P_s variation for $\varepsilon_\mu^{p\,max}$ up to 0.12. Concerning the third macroscopic parameter $\frac{\triangle V}{V_0}$, Figure 9 shows that this parameter depends only on E_μ^t and $\varepsilon_\mu^{p\,max}$ and it is effectively independent of σ_μ^d.

After studying the influence of the microscopic parameters on the macroscopic densification behavior, calibration becomes fairly easy. Because the macroscopic densification pressure P_d depends only on the microscopic one σ_μ^d, this parameter must be calibrated first. Subsequently, the microscopic tangent modulus E_μ^t can be calibrated to ensure the expected value of the macroscopic saturation pressure. Finally, the maximum permanent deformation of the beam bonds $\varepsilon_\mu^{p\,max}$ can be set to find the appropriate global volume change. Table 3 gives the calibrated microscopic densification parameters that must be used to ensure the correct macroscopic densification behavior of silica glass.

2.2.3. Validation

This subsection attempts to validate the microscopic densification parameters obtained by calibration (**Table 3**). The same geometric model as for the calibration study is used in this section. The various microscopic densification parameters of cohesive beams are set as indicated in Table 3. This model is subjected to various hydrostatic
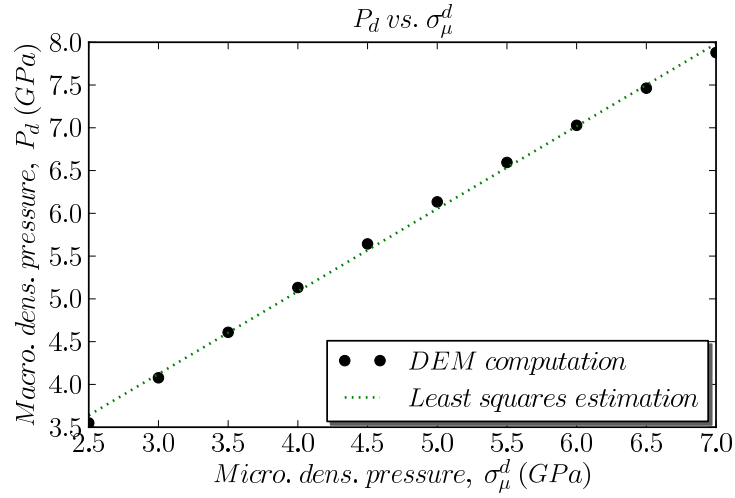
(a) $E_\mu^t = 0\,GPa$, $\varepsilon_\mu^p = 0.05$
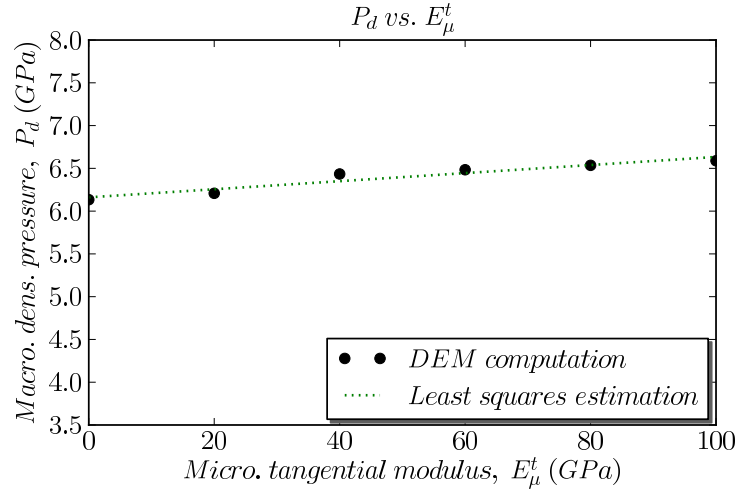
(b) $\sigma_\mu^d = 5\,GPa$, $\varepsilon_\mu^p = 0.05$
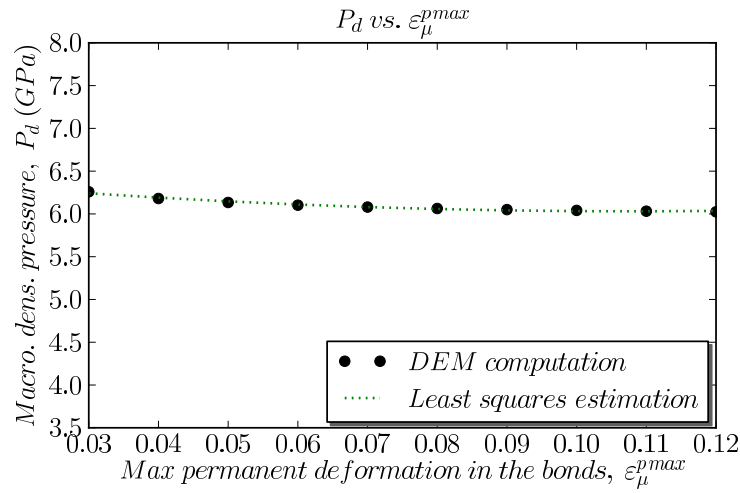
(c) $\sigma_\mu^d = 5\,GPa$, $E_\mu^t = 0\,GPa$

Figure 7: Variation of macroscopic densification pressure (P_d) with the microscopic densification parameters: microscopic densification pressure (σ_μ^d), microscopic tangential modulus (E_μ^t) and maximum permanent deformation of the beam bonds ($\varepsilon_\mu^{p\,max}$)

Figure 8: Variation of macroscopic saturation pressure (P_s) with microscopic densification parameters: microscopic densification pressure (σ_μ^d), microscopic tangential modulus (E_μ^t) and maximum permanent deformation of the beam bonds ($\varepsilon_\mu^{p\,max}$)
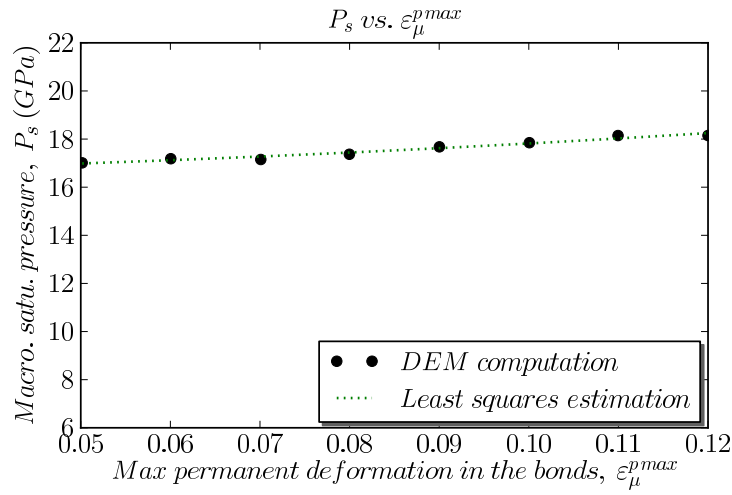
Figure 9: Variation of volume change ($\frac{\Delta V}{V_0}$) with microscopic densification parameters: microscopic densification pressure (σ_μ^d), microscopic tangential modulus (E_μ^t) and maximum permanent deformation of the beam bonds ($\varepsilon_\mu^{p\,max}$)
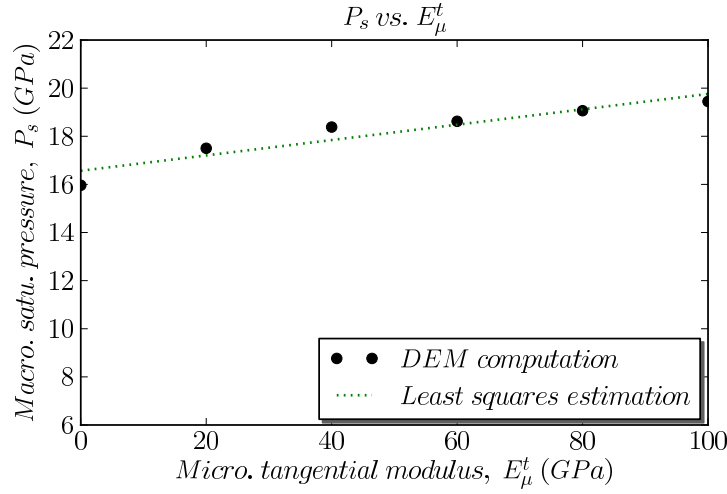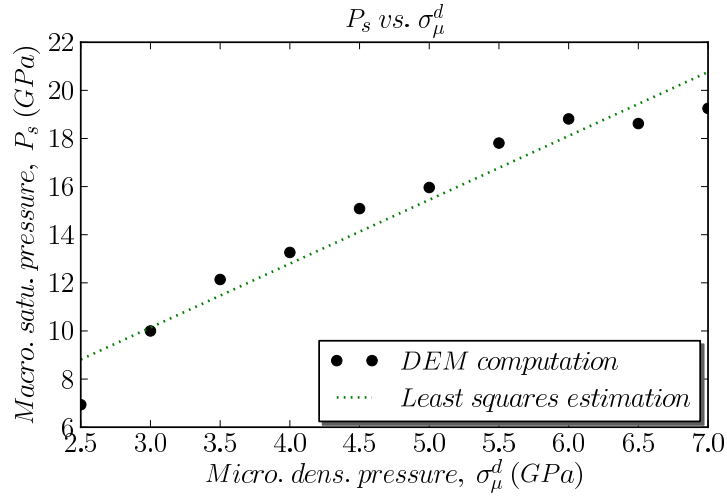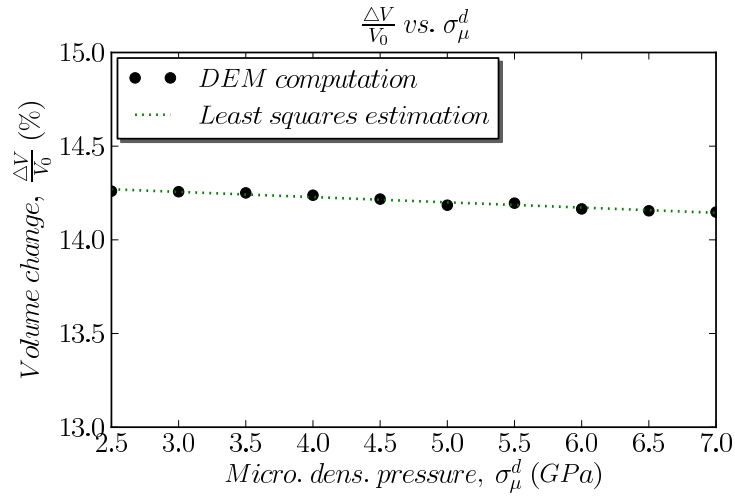
Table 3: The microscopic densification parameters of silica glass (obtained by calibration)

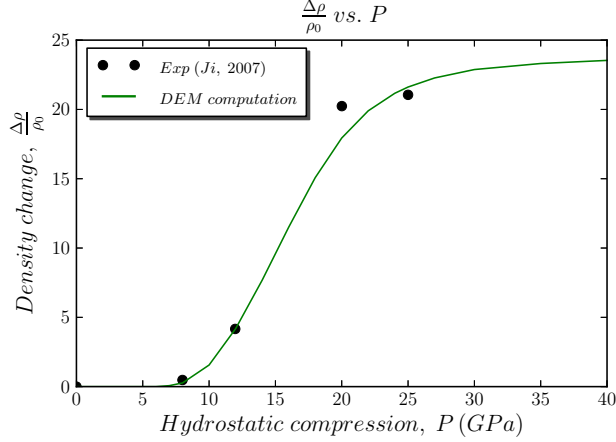| Micro. dens. pressure	Micro. tangential modulus	Max permanent def in the bonds
$\sigma_\mu^d = 7.13\,GPa$	$E_\mu^t = 98.82\,GPa$	$\varepsilon_\mu^{p\,max} = 0.067$

Figure 10: Density change with pressure: comparison between experimental [8, 9] and numerical results.

pressures. The associated permanent deformations are measured and compared to Ji's [8] experimental results (**Fig. 10**). As can be observed in Figure 10, the numerical results are in agreement with the experimental ones.

3. Fracture

The approaches most commonly used to model fracture in discrete methods, e.g. DEM [18, 19], are based on the computation of bond strain [28] or stress [29]. The bond breaks if the associated strain (or stress) exceeds a given value, generally determined by calibration tests. On the macroscopic scale, this criterion is moderately satisfactory [19]. However, on the microscopic scale, it cannot reproduce correctly the cracking mechanisms [20]. Recently, another criterion based on the computation of an equivalent of the stress tensor at each particle has been proposed by André *et al.* [20]. This criterion is detailed in the remainder of this section.

The equivalent Cauchy stress is computed with the help of the notion of virial stress which is the most commonly used definition of stress in discrete particle systems, particularly in Molecular Dynamics (MD) [21]. This "stress" includes two parts [21]: the first part depends on the mass and the velocity (or, in some versions, the fluctuation of the velocity) of particles; the second part depends on inter-particle forces and particle positions, providing a continuum measure for the internal mechanical interactions between particles. In this definition, the average virial stress over a volume Ω around a particle i is given by (7)

$$\bar{\mathbf{\Pi}} = \frac{1}{\Omega}\left(-m_i\,\dot{\boldsymbol{u}}_i \otimes \dot{\boldsymbol{u}}_i + \frac{1}{2}\sum_{j \neq i} \boldsymbol{r}_{ij} \otimes \boldsymbol{f}_{ij}\right) \tag{7}$$

where m_i and $\dot{\boldsymbol{u}}_i$ are, respectively, the mass and the velocity of the particle i, $\boldsymbol{r}_{ij} = \boldsymbol{r}_j - \boldsymbol{r}_i$, $\boldsymbol{r}_i$ is the position vector of particle i, $\boldsymbol{f}_{ij}$ is the inter-particle force acting on particle i exerted by particle j and $\otimes$ denotes the tensor product. The virial stress (7) is widely used to compute an equivalent of Cauchy stress in discrete systems. Recently, Zhou [22] demonstrated that this quantity is not a measure for mechanical forces between material points and cannot be regarded as a measure of mechanical stress. Zhou proposed another formulation to compute the average mechanical

stress, including only the second part of (7). For a region Ω around a particle i, the average stress is:

$$\bar{\sigma} = \frac{1}{2\Omega} \sum_{i\in\Omega} \sum_{j\neq i} r_{ij} \otimes f_{ij} \tag{8}$$

The expressions (7) and (8) are developed for Molecular Dynamics (MD), where the inter-particle forces are a function of the Lennard-Jones potential $\Phi(r_{ij})$ and the distance between the particles. In this instance, the two expressions of stress (7) and (8) lead to symmetric tensors. However, this cannot be generalized to all other discrete models. The variation of the DEM used here, where the particles are linked by cohesive beams, does not ensure the symmetry condition of the resulting tensors. André *et al.* [20] proposed a slight modification of (8) to restore the symmetry condition of the stress tensor as follows:

$$\bar{\sigma} = \frac{1}{2\Omega} \sum_{i\in\Omega} \sum_{j\neq i} \frac{1}{2}(r_{ij} \otimes f_{ij} + f_{ij} \otimes r_{ij}) \tag{9}$$

An equivalent Cauchy stress tensor for each discrete element i is computed using (9), where $\Omega = \Omega_i$, the volume of i (10).

$$\bar{\sigma}_i = \frac{1}{2\Omega_i} \sum_{j\neq i} \frac{1}{2}(r_{ij} \otimes f_{ij} + f_{ij} \otimes r_{ij}) \tag{10}$$

According to Griffith theory [30, 31], the fracture of brittle solids initiates under tensile stress. Therefore, the new criterion postulates that a discrete element i is released from its neighbors when the hydrostatic stress ($\bar{\sigma}_i^{hyd} = \frac{1}{3} trace(\bar{\sigma}_i)$) is positive (tension state in i) and exceeds the microscopic fracture strength (σ_f^{hyd}). In this case, all the beam bonds linking this particle to its neighbors break and do not intervene any more to compute the inter-particle forces and torques in the next time step. The microscopic fracture strength of silica glass, determined by calibration tests, is $\sigma_f^{hyd} = 67\,MPa$.

4. Vickers indentation

As shown previously, silica glass experiences permanent densification under high compressive pressure. Comparable hydrostatic stresses can be reached beneath a sharp indenter during indentation loading. This section studies Vickers indentations in silica glass using various levels of indentation forces. First, low indentation forces are used to study the densification behavior at micro-scales (without fracture). Subsequently, high indentation forces are used to study to densification influence on the cracking behavior of silica glass.

A hemispherical model with a radius of $12\,\mu m$ is used for the Vickers indentation studies (**Fig. 11**). This model, whose the spherical part (dome) is fixed, is discretized using $N_p = 100\,000$ discrete elements (i.e., the average radius of the discrete elements is around $0.2\,\mu m$) to capture the microscopic mechanisms of the densification. It is indented with a square-based pyramidal indenter having included face angles of $136°$ (Vickers indenter) and $2\,\mu m$ in height (**Fig. 11**). This indenter undergoes a moderate displacement in the z direction until the reacting force reaches the desired indentation force.

Table 4 presents a comparison between the experimental [8, 32] and the present numerical indentation results for low indentation forces ($F_{indent} = 0.1\,N$ and $F_{indent} = 0.5\,N$).

For $F_{indent} = 0.1\,N$, the DEM simulation yielded a relatively good estimate of the volume of the indentation print V^- and the volume of the piled-up material around the indenter V^+. The densified volume V^d which is a function of V^- and V^+ compare favorably with the experimental results [32, 8] (in comparison to previous numerical studies [8]). Furthermore, a good numerical result was obtained for the diagonal length of the indentation print (L) which is used to compute the hardness. However, the indentation depth D was low compared with the experimental results [32, 8]. This can be explained by the fact that in the experimental tests, micro-cracks can initiate under the indenter tip (zone of high stress concentration), causing measurement errors in D. The experimental value of D can includes not only the depth of the indentation but also the depth of the crack.
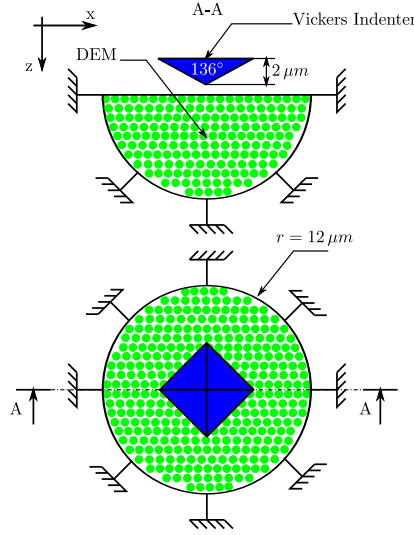
Figure 11: DEM indentation model

For $F_{indent} = 0.5\,N$, the densification state becomes more significant and a far greater densification print is obtained (**Fig. 13**). Compared with the experimental results, the DEM numerical simulation provided a relatively good estimate of the volume of the piled-up material around the indenter V^+ and the diagonal length L of the indentation print. Concerning D, the analysis of the $F_{indent} = 0.1\,N$ case remains valid. However, this time, the volume of indentation print V^- is slightly high. This can be explained by the side-effects. In the case of $F_{indent} = 0.5\,N$, the densified zone is relatively important compared with the global geometric model. Consequently, the effects of the overstated fixation conditions applied to the dome (the spherical part of the geometric model) become significant. This can increase the region where the densification pressure P_d can be reached and then V^-.

One way to reduce the side effects is to use larger domains. However, such a solution can amplify considerably the computational time, because a very fine discretization must be applied to capture the microscopic densification effects. To circumvent the computational time problem, the discrete-continuum coupling model is used, a hybrid between the discrete element method and the constrained natural element method (CNEM-DEM coupling) [23]. The discrete element model is applied in the indentation region where the densification pressure (P_d) can be reached, whereas the continuum model (CNEM) is applied over the remainder of the body being modeled. Figures 12 presents the coupling model which is a box of $30\,\mu m$ on each side. The discrete subdomain where the DEM is applied is the same as in the previous study (DEM computation). The remainder of the box is modeled using CNEM and discretized with $10\,000$ nodes. A $2\,\mu m$-thick bridging zone is used between these two models to ensure correct wave propagation between them. Because the CNEM domain is far from the indentation region, it will experience only elastic deformations. Therefore, only the elastic behavior is modeled in this region.

As shown in Table 4, in the case of $F_{indent} = 0.1\,N$, the DEM and CNEM-DEM coupling results are practically the same. However, in the case of $F_{indent} = 0.5\,N$ where the side-effects became significant, the CNEM-DEM coupling results are better than those obtained using the discrete model (DEM) only. Furthermore, the CNEM-DEM coupling improved the shape of the densified zone as shown in Figure 14 which presents a cut-away view of the indented model in the case of $F_{indent} = 0.5\,N$. It can be observed that the densified zone obtained from the coupling method (**Fig. 14c**) is closer to Ji's experimental results (**Fig. 14a**) [8] than the densified zone obtained from the DEM computations (**Fig. 14b**). Indeed, it is less deep and broader in the former (coupling result) than in the latter (DEM result).

The previous paragraph showed that the densification model, developed in this work, gives a relatively good quantitative estimate of silica glass densification at micro-scales when low indentation forces are applied (in comparison to previous numerical studies [8]). Next, a high indentation force ($F_{indent} = 30\,N$) is applied to study the influence of densification on silica glass cracking behavior.
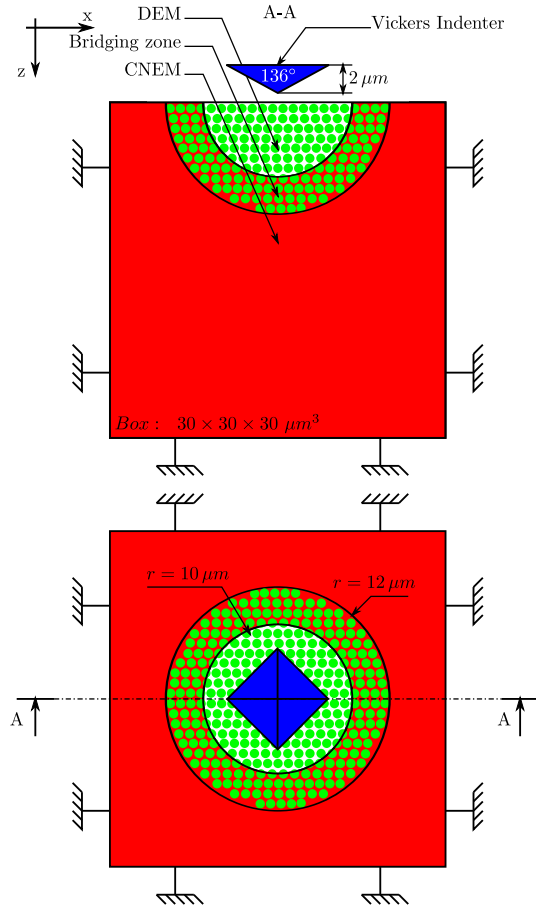
Figure 12: CNEM-DEM coupling indentation model
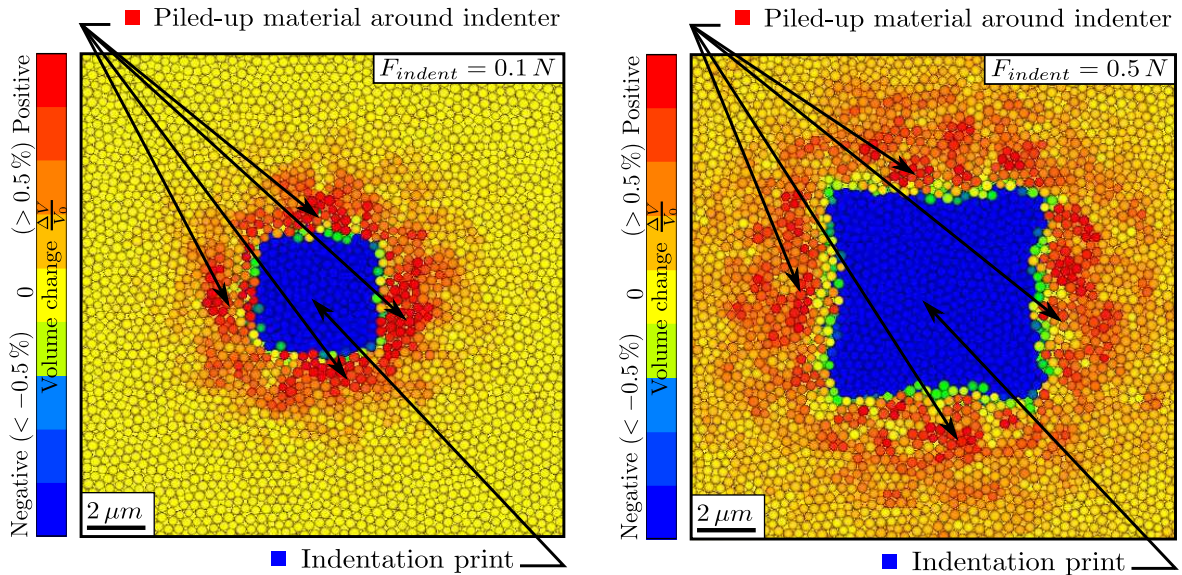
Figure 13: Top view of indentation print (blue: negative volume change) and piled-up material around indenter (red: positive volume change). Left: indentation force $F_{indent} = 0.1\,N$; right: indentation force $F_{indent} = 0.5\,N$.

(a) Experimental results (Ji, 2007)

(b) DEM numerical results

(c) CNEM-DEM numerical results

Figure 14: Cut-away view of the indented region; $F_{indent} = 0.5\,N$; top: experimental results from Ji [8], middle: DEM numerical results; bottom: CNEM-DEM coupling numerical result

Table 4: Vickers indentation results: low indentation forces

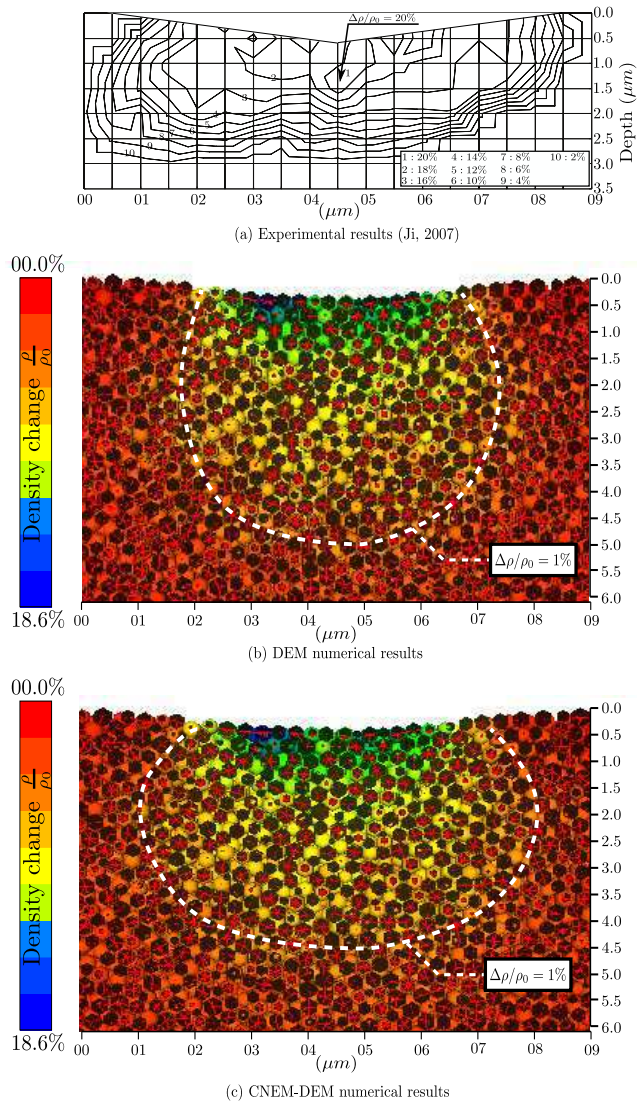|		$V^- \, (\mu m^3)$	$V^+ \, (\mu m^3)$	$V^d \, (\mu m^3)$	$D \, (\mu m)$	$L \, (\mu m)$
$F_{indent} = 0.1\,N$	Num (DEM): Present	1.304	0.136	1.168	0.159	4.758
	Num (CNEM-DEM): Present	1.302	0.131	1.171	0.159	4.758
	Num [8]	––	––	0.058	––	––
	Exp [8]	0.727	0.108	0.605	0.377	4.707
	Exp [32]	1.034	0.018	0.952	0.421	5.157
$F_{indent} = 0.5\,N$	Numerical (DEM)	14.534	1.174	13.360	0.397	9.318
	Numerical (CNEM-DEM)	13.628	0.920	12.708	0.409	9.957
	Num [8]	––	––	0.61	––	––
	Exp [8]	9.971	1.138	8.805	0.908	10.371
/	Experimental error [8]	±4%	±7%	±10%	±6%	±2%

V^- and V^+ are, respectively, the volumes of the indentation print and of the piled-up material around the indent, V^d is the densified volume, D is the indentation depth and L is the diagonal length of the indentation print.

A model similar to the one presented in Figure 11 is used for this study. Because the indentation force is high, the region where the densification pressure P_d can be reached becomes large. Hence, the radius of the model is increased to $120\,\mu m$. As shown in previous studies [33, 34], brittle materials indented with a spherical indenter produce a cone crack. However, when a Vickers tip is used, normal glasses produce median, radial and lateral cracks. Instead, silica glass has a strong tendency to form a cone crack, even when indented with a Vickers tip. Because of its important densification behavior, a spherical densified zone is formed beneath the Vickers indenter which in turn operates as a spherical indenter, so that a cone crack is set up that can accompany median, radial and lateral cracks. Figure 15 presents the numerical cracking response of silica glass indented with a Vickers tip at the beginning of fracture (before the cracking becomes unstable). In this figure, only the discrete elements where the fracture criterion is reached are shown. Qualitatively, the result is in good agreement with those obtained in other studies [6, 5]. Moreover, the radius of the cone crack obtained numerically ($r_{num}^{cone} = 41.14\,\mu m$) is in good agreement with the experimental works of Arora *et al.* [6] ($r_{exp}^{cone} \approx 40\,\mu m$).

5. Conclusion

This paper attempted to reproduce numerically the anomalous behavior of silica glass and increase the comprehension of this behavior. Understanding permanent deformations in this type of glass represents a considerable challenge. An assumption has been made that the densification takes place only under high compressive pressure and that no shearing stresses influence the final permanent deformation levels. Based on this assumption, a densification model, adapted for discrete element methods, is developed in this work. The densification behavior is modeled by a "spring-slider" system incorporated between beam-linked particles at the micro scale. This system activates only under compression stress. The densification model involves three microscopic parameters which can be determined by calibration tests. As shown previously, the calibration process of these parameters is fairly easy. The macroscopic densification pressure P_d is a linear function of microscopic densification pressure σ_μ^d only. Therefore, σ_μ^d can be determined independently from the other microscopic parameters. Subsequently, the microscopic tangential modulus can be calibrated taking into account the macroscopic saturation pressure P_s. Finally, the maximum permanent deformation can be set to adjust the macroscopic volume change $\frac{\Delta V}{V_0}$ (or the density change $\frac{\Delta \rho}{\rho_0}$). It is shown that, after calibration, this model gives good macroscopic densification results compared with those obtained experimentally (**Fig. 10**). To validate this model at microscopic scales, simulations of the Vickers indentation process were performed with three different indentation forces. First, low forces ($0.1\,N$ and $0.5\,N$) were used to validate microscopically the densification model in the absence of fracture. A comparison of these results

(a) Experimental result (Arora, 1979)

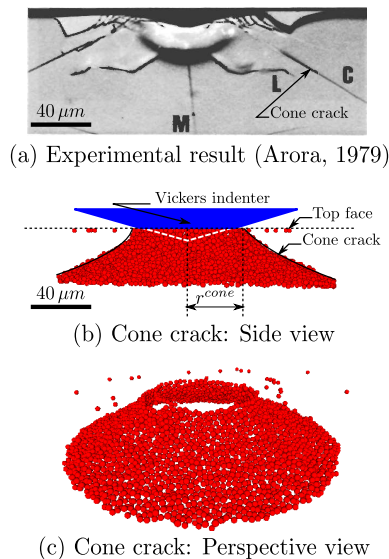(b) Cone crack: Side view

(c) Cone crack: Perspective view

Figure 15: Cracking pattern of silica glass indented with a Vickers tip; $F_{indent} = 30\,N$; only the discrete elements where the fracture criterion is reached are shown in (b) and (c).

with experimental ones [8] shows that this model is also validated at microscopic scales (when microscopic loading is applied) and represents an advancement in the comprehension of permanent deformation in silica glass.

The influence of the densification behavior on the cracking response was studied by applying a high indentation force ($30\,N$). As can be observed in Figure (**Fig. 15**), the silica glass forms primarily a cone crack. This is due to the densification behavior, which leads to the formation of a spherical densified region. This, in turn, behaves as a spherical indenter that will induce in most brittle materials a cone crack at the beginning of fracture. When the indentation force further increases, other types of cracking appear and induce the complete destruction of the sample.

The developments in this work have been implemented in the GranOO workbench, which now provides a robust numerical tool to simulate brittle continuous media. For more details, the reader is referred to http://www.granoo.org.

References

[1] R. Brückner, J. Non-Cryst. Solids 5 (1970) 123.

[2] R. Brückner, J. Non-Cryst. Solids 5 (1971) 177.

[3] V. Le Houérou, J. C. Sangleboeuf, S. Dériano, T. Rouxel, G. Duisit, J. Non-Cryst. Solids 316 (2003) 54.

[4] T. Rouxel, J. C. Sangleboeuf, J. Non-Cryst. Solids 271 (2000) 224.

[5] T. Gross, J. Non-Cryst. Solids 358 (2012) 3445.

[6] A. Arora, D. Marshall, B. Lawn, M. Swain, J. Non-Cryst. Solids 31 (1979) 415.

[7] P.W. Bridgman, I. Šimon, J. Appl. Phys. 24 (1953) 405.

[8] H. Ji, Mécanique et physique de l'indentation du verre , Ph.D. thesis, Université de Rennes 1 (2007).

[9] H. Ji, V. Keryvin, T. Rouxel, T. Hammouda, Scr. Mater. 55 (2006) 1159.

[10] T. Rouxel, H. Ji, T. Hammouda, A. Moréac, Phys. Rev. Lett. 100 225501 (2008).

[11] H. Cohen, R. Roy, J. Am. Ceram. Soc. 44 (1961) 523.

[12] C. Weir, S. Spinner, J. Am. Ceram. Soc. 45 (1962) 196.

[13] H. Cohen, R. Roy, J. Am. Ceram. Soc. 45 (1962) 398.

[14] V. Keryvin, Contribution à l'étude des mécanismes de déformation et de fissuration des verres, habilitation à diriger des recherches, Université de Rennes 1 (2008).

[15] T. Rouxel, H. Ji, F. Augereau, B. Rufflé, J. Appl. Phys. 107 094903 (2010).

[16] E. Christiansen, S. Kistler, W. Gogarty, J. Am. Ceram. Soc. 45 (1962) 172.

[17] J. Mackenzie, J. Am. Ceram. Soc. 46 (1963) 461.

[18] D. André, I. Iordanoff, J. Charles, J. Néauport, Comput. Meth. Appl. Mech. Eng. 213-216 (2012) 113.

[19] D. André, Modélisation par éléments discrets des phases d'ébauchage et de doucissage de la silice, Ph.D. thesis, Université Bordeaux 1 (2012).

[20] D. André, M. Jebahi, I. Iordanoff, J. L. Charles, J. Néauport, under review in Comput. Meth. App. Mech. Eng (2013).

[21] A. McLellan, Am. J. Phys. 42 (1974) 239.

[22] M. Zhou, Proc. R. Soc. Lond. A 459 (2003) 2347.

[23] M. Jebahi, J. Charles, F. Dau, L. Illoul, I. Iordanoff, Comput. Meth. App. Mech. Eng. 255 (2013) 196.

[24] S. Timoshenko, History of Strength of Materials: With a Brief Account of the History of Theory of Elasticity and Theory of Structure, Dover, New York, 1983.

[25] G. Kanel, J. Mech. Phys. Solids 35 (1998) 1869.

[26] J. Lubliner, Plasticity theory, Dover, New York, 2008.

[27] C. Zha, R. Hemley, H. Mao, T. Duffy, M. Charles, Phys. Rev. B 50 (1994) 13105.

[28] H. A. Carmona, F. K. Wittel, F. Kun, H. J. Herrmann, Phys. Rev. E 77 051302 (2008).

[29] D. O. Potyondy, P. A. Cundall, Inter. J. Rock Mech. Min. Sci. 41 (2004) 1329.

[30] A. Griffith, Phil. Trans. R. Soc. Lond. A 221 (1921) 163.

[31] K. Muralidharan, J. Simmons, P. Deymier, K. Runge, J. Non-Cryst. Solids 351 (2005) 1532.

[32] S. Yoshida, J. Sangleboeuf, T. Rouxel, J. Mater. Res. 20 (2005) 3404.

[33] H. Hertz, Hertz's Miscellaneous Papers, Vol. 55, Macmillan, 1896, Ch. On the contact of elastic solid, 1881. doi:10.1038055006f0.

[34] H. Hertz, Hertz's Miscellaneous Papers, Vol. 55, Macmillan, 1896, Ch. On hardness, 1882. doi:10.1038055006f0.

[35] A. Polian, Phys. Rev. B 47 (1993) 13979.

[36] Zha, C. S., R. J. Hemley, H. K. Mao, T. S. Duffy, C. Meade, Phys. Rev. B 50 (1994) 13105.